A MEMS *XY*-stage integrating compliant mechanism for nanopositioning at sub-nanometer resolution

2016 J. Micromech. Microeng. 26 025014

(http://iopscience.iop.org/0960-1317/26/2/025014)

IOP Publishing Journal of Micromechanics and Microengineering
J. Micromech. Microeng. **26** (2016) 025014 (9pp) doi:10.1088/0960-1317/26/2/025014

A MEMS *XY*-stage integrating compliant mechanism for nanopositioning at sub-nanometer resolution

Xiang Xi[1,2], Tyler Clancy[1], Xuezhong Wu[2], Yu Sun[3] and Xinyu Liu[1]

[1] Department of Mechanical Engineering, McGill University, QC H3A 0G4, Canada
[2] Department of Mechatronics Engineering, National University of Defense Technology, Hunan 410073, People's Republic of China
[3] Department of Mechanical and Industrial Engineering, University of Toronto, Toronto ON M5S, Canada

E-mail: xinyu.liu@mcgill.ca

Received 28 August 2015, revised 26 October 2015
Accepted for publication 8 December 2015
Published 11 January 2016

Abstract

This paper reports a microelectromechanical systems (MEMS) based *XY*-stage integrating compliant motion amplification mechanism for nanopositioning at sub nanometer resolution. The MEMS stage is driven by bidirectional Z-beam electrothermal actuators that generate large output forces to actuate the motion amplification mechanism. The motion amplification mechanisms are used in their inverse (motion reduction) mode to convert micrometer input displacements (from the Z-beam actuators) into nanometer output displacements at a constant motion reduction ratio with good linearity. This unique design significantly enhances the positioning resolution of the *XY*-stage. An analytical model is developed to predict output displacements of the *XY*-stage as a function of the input voltages applied to the Z-beam actuators, and the predicted results agree with the experimental results. Capacitive displacement sensors are arranged along both *X*- and *Y*-axes for measuring the input displacements of the amplification mechanisms, enabling closed-loop nanopositioning control of the *XY*-stage. The device calibration results show that, within an actuation voltage of ± 15 V, the MEMS stage offers a motion range close to ± 1 μm and a displacement resolution better than 0.3 nm $\sqrt{\text{Hz}}^{-1}$.

Keywords: microelectromechanical systems (MEMS) *XY*-stage, compliant mechanism, motion amplification mechanism, nanopositioning, Z-beam electrothermal actuator, capacitive displacement sensor

(Some figures may appear in colour only in the online journal)

1. Introduction

Nanopositioning stages, capable of producing high-precision motions with nanometer resolutions, represent an enabling tool in micro and nanotechnology with many important applications [1]. For instance, conventional large-sized piezoelectric nanopositioning stages have been widely used in scanning probe microscopy (SPM) for positioning a sample under a scanning probe in nanometer-sized raster patterns [2]. With the advancement of microelectromechanical systems (MEMS), MEMS nanopositioning stages have also been developed with appealing advantages such as small footprint, low power consumption, fast dynamics, and low unit cost [3–5]. These MEMS devices are mainly applied to optical scanning [6, 7], SPM sample scanning [8–10], micro- and nanomanipulation [11–14], and probe-based high-density data storage [15–17].

According to their output motions, MEMS nanopositioning stages fall into three categories: translational (*XY* and *XYZ*) [4, 6, 7, 9], torsional (micromirrors) [3, 18], and combinational (translational plus torsional) [19, 20] stages. This paper will be focused on MEMS *XY*-stages for in-plane

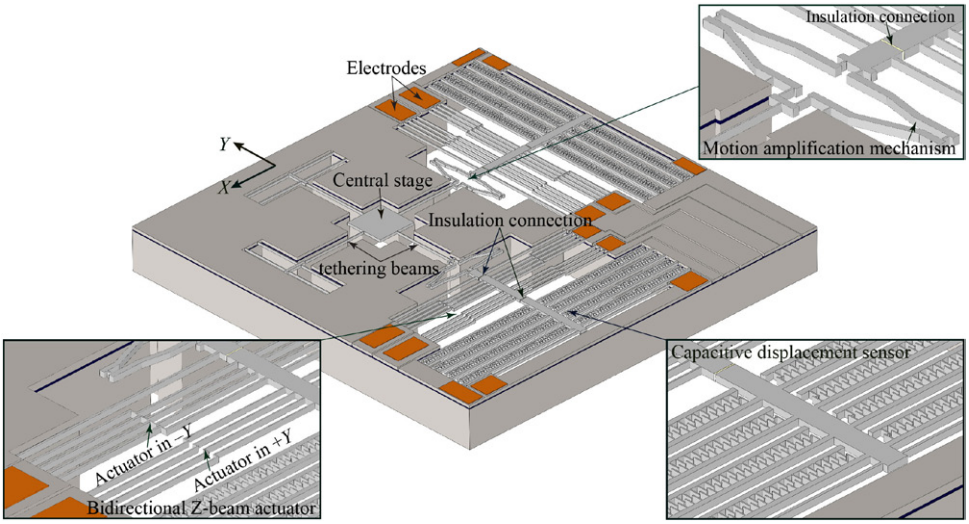

Figure 1. Schematic of the MEMS nanopositioning *XY*-stage.

translational nanopositioning. There has been a vast literature reporting MEMS *XY*-stages [4, 6, 13, 15, 21]. The positioning resolution of MEMS stages is mainly determined by the actuation mechanism, and existing MEMS *XY*-stages commonly employed electrostatic comb-drive [6, 12, 13, 15] or electrothermal [21–23] actuators. The electrostatic comb-drive actuation is more popular in *XY*-stage designs, which provides nanometer positioning resolution and fast dynamic response [10, 11, 24]; however, it has relatively small output forces (e.g. within the range of hundreds of micronewtons for bulk-micromachined devices) and usually requires large actuation voltages (up to >100 V) [13]. The MEMS *XY*-stages with comb-drive actuators provide typical open-loop positioning resolution at the order of 1–10 nm $\sqrt{\text{Hz}}^{-1}$.

For nanopositioning applications that require larger output forces (e.g. >1 mN), electrothermal actuators are more appropriate for actuation of MEMS *XY*-stages. The classical V-beam electrothermal actuators have been employed in some MEMS *XY*-stages [21–23], which produce millinewton-level output forces at an actuation voltage of <10 V. Recently, electrothermal actuators with Z-shaped thermal expansion beams (which are called Z-beam actuators) were also developed and used in MEMS *XY*-stages [25–28]. The Z-beam actuator has lower axial stiffness than the V-beam actuator, and thus allows for bidirectional actuation. Due to the inherent nature of thermal actuation, all the MEMS *XY*-stages with electrothermal actuators have lower open-loop positioning resolution than the electrostatic actuators.

To further enhance the positioning resolution, some MEMS *XY*-stages also integrated high-precision, on-chip displacement sensors for closed-loop controlled nanopositioning. The adopted displacement sensing mechanisms include capacitive [24], piezoresistive [12], and electrothermal sensing [10], and the typical sensing resolution is at the order of 1 nm $\sqrt{\text{Hz}}^{-1}$. A recently reported position sensing technique for MEMS *XY*-stages employed an inductor-capacitor (LC) circuit for high-resolution capacitance measurement, and achieved an enhanced resolution of 0.008 nm $\sqrt{\text{Hz}}^{-1}$[29]. However, this technique requires the use of a high-frequency lock-in amplifier, making the whole experimental setup relatively sophisticated.

This paper proposes a new design of MEMS *XY*-stage that provides enhanced sub-nanometer positioning resolution. The novelty of the *XY*-stage design lies in the integration of a compliant motion amplification mechanism (operated in its inverse mode for motion reduction) and a bidirectional Z-beam electrothermal actuator along each axis. The motion amplification mechanism is used for linearly converting large input displacements (micrometers)—generated by the Z-beam actuator—into small output displacements (nanometers to sub-nanometers) for achieving enhanced sub-nanometer positioning resolution. In the meanwhile, the inverse operation of the amplification mechanisms also leads to the amplification of millinewton output forces from the Z-beam actuator to an even higher level for heavy-load nanopositioning. Analytical modeling and finite element simulation of the *XY*-stage are conducted to provide device design guidelines. Calibration and closed-loop nanopositioning control of the *XY*-stage are performed to demonstrate the device performance.

2. Device design and analysis

2.1. Working principle and microfabrication

The schematic of the proposed MEMS *XY*-stage is shown in figure 1. Along each in-plane axis (*X* and *Y*), the stage integrates a motion amplification mechanism, a bidirectional Z-beam electrothermal actuator, and a capacitive displacement sensor. In the bidirectional actuator, two groups of Z-shaped beams (Z-beams) are arranged facing each other; upon electrical actuation of one group of Z-beams, Joule-heating-induced thermal expansions bend the Z-beams and drive the central shaft of the actuator moving forward, during which the other group of un-actuated Z-beams are bent reversely because of their low axial stiffness [28]. The Z-beam actuator produces bidirectional displacements, which are linearly reduced by the motion amplification mechanism by a constant factor (motion reduction ratio). The reduced output displacement from the

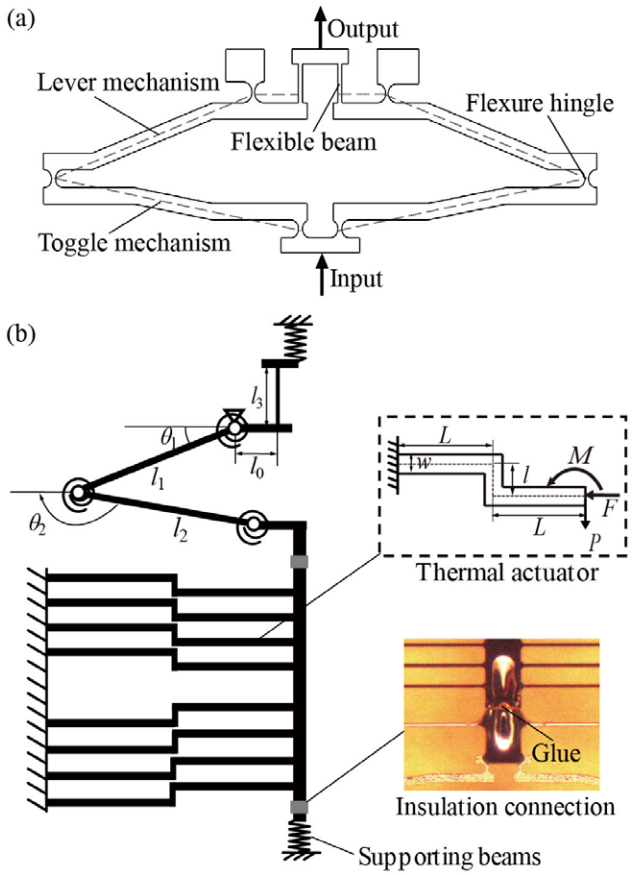

Figure 2. Theoretical model of the MEMS stage.

motion amplification mechanism is finally transmitted to a central stage through a tethering beam. The capacitive displacement sensor with interdigitated comb fingers is used to measure the input displacement of the motion amplification mechanism, enabling closed-loop position control of the *XY*-stage. The good linearity of the motion amplification mechanism (data presented in section 3) guarantees the accurate prediction of the output displacement at the central stage based on the position feedback from the capacitive displacement sensor. The central stage is suspended by four tethering beams along the *X*- and *Y*-axes, and the orthogonal configuration of the two actuators minimizes the cross-coupling of the *X*- and *Y*-axis motions of the stage [13].

Compliant motion amplification mechanisms have been widely used in MEMS designs mainly for amplifying motions [30–32]. When high positioning resolution is more concerned than a large motion range, the motion amplification mechanism can be used in its inverse mode for motion reduction [33]. As an additional advantage, the output force can be also amplified by the same factor as motion reduction. In this work, we utilize this motion reduction strategy for enhancing the positioning resolution of the MEMS *XY*-stage. The motion amplification mechanism employed in this design, as shown in figure 2(a), includes two typical motion amplification mechanisms: toggle mechanism and lever mechanism, which are connected in series and reduce the input displacement by two stages. The input end, the toggle and lever mechanisms are connected by single-axis torsional flexure hinges, and the output end is connected by a thin flexible beam. The toggle mechanism provides a large motion amplification/reduction ratio with a simple and compact structure, thus allowing the two-stage motion amplification mechanism to have a large overall amplification/reduction ratio in a small footprint [34].

The *XY*-stage was fabricated using the SOIMUMPs foundry process (MEMSCAP Inc.) with a 25 μm thick device layer. Since the SOIMUMPs process does not allow for deep-trench electrical isolation of the device layer connected by the buried and handle layers [35], two 5 μm gaps were fabricated in the suspended shaft of each axis to electrically isolate the motion amplification mechanism, the Z-beam actuator, and the capacitive displacement sensor (figure 1). After device fabrication, micro-drops of UV-curable dielectric epoxy glue (Loctite® 3335), which has high strength at elevated temperature, were added to the gaps using a glass microneedle, and hardened using a UV lamp for 1 min (4 W) to form electrically-insulated mechanical connections (photographic inset in figure 2(b)).

2.2. Analytical modeling

In order to provide a systematic design approach for determining structural parameters of the *XY*-stage, an analytical model needs to be derived. The analytical models of the Z-beam actuator and the motion amplification mechanism have been developed in previous studies [26, 33]. Here, we briefly introduce these existing models, based on which an overall model of the *XY*-stage is synthesized for design of the device parameters. Since the two axes of the *XY*-stage are structurally identical and motion-decoupled, the mechanism along only one axis is analyzed. Figure 2(b) illustrates the geometric parameters of the *XY*-stage along one axis. The motion reduction ratio of the amplification mechanism is [33]

$$\alpha = -\frac{l_0}{l_1(\cos\theta_1 - \sin\theta_1 \cot\theta_2)} \tag{1}$$

where l_0, l_1 and θ_1, θ_2 are beam lengths and angle parameters of the amplification mechanism, respectively.

To derive the output displacement of the single-axis stage, a single Z-shaped beam with equivalent boundary conditions (schematic inset in figure 2(b)) is analyzed using the energy method, yielding a closed-form equation that describes three reaction forces/moments at the guided end of the Z-shaped beam—axial force *F*, virtual force *P*, and moment *M* [26] :

$$\begin{bmatrix} f_{11} & f_{12} & f_{13} \\ & f_{22} & f_{23} \\ \text{symmetric} & & f_{33} \end{bmatrix} \begin{bmatrix} F \\ P \\ M \end{bmatrix} = \begin{bmatrix} 2\gamma\Delta T \\ U \\ 0 \end{bmatrix} \tag{2}$$

where γ is the thermal expansion coefficient of silicon, U is the output displacement of the Z-beam actuator, ΔT is the average temperature increase on the Z-shaped beam, which can be calculated by [36]

$$\Delta T = \frac{V^2}{12\kappa\rho} \tag{3}$$

where V is the voltage loading, κ is the thermal conductivity of silicon, and ρ is the resistivity of silicon. The coefficient matrix in equation (2) can be expressed by the geometric and material parameters [26]:

$$f_{11} = \frac{2l}{EA} + \frac{l^3}{3EI} + \frac{Ll^2}{EI}, f_{12} = \frac{3L^2l}{2EI} + \frac{Ll^2}{2EI},$$
$$f_{13} = -\frac{l^2}{2EI} - \frac{Ll}{EI}, f_{22} = \frac{l}{EA} + \frac{Ll^2}{EI} + \frac{8L^3}{3EI},$$
$$f_{23} = -\frac{2L^3}{EI} - \frac{Ll}{EI}, f_{33} = \frac{2L}{EI} + \frac{l}{EI} \quad (4)$$

where E is the Young's modulus of silicon, L and l are two length parameters of the Z-shaped beam (schematic inset in figure 2(b)), and A and I are the cross-sectional area and moment of inertia of the Z-shaped beam, respectively.

The virtual force P reflects the total stiffness of loading structures (K) connected to the actuator shaft, which includes the stiffness of eight unactuated Z-shaped beams (K_Z) and four fixed-guided supporting beams for the actuator shaft (K_S), and the input stiffness of the motion amplification mechanism (K_m):

$$P = -\frac{1}{8}KU = -\frac{1}{8}(K_Z + K_S + K_m)U \quad (5)$$

where the factor of 1/8 reflects the load distribution over the eight actuating Z-shaped beams.

The stiffness of eight Z-shaped beams is [26]:

$$K_Z = \frac{8Ew^3h(l^3 + 2Lw^2 + 6Ll^2)}{8L^3l^3 + w^2l^4 + 16w^2L^4 + 2w^4Ll + 12L^4l^2 + 6w^2Ll^3} \quad (6)$$

where w and h is the width and height of the beam. The stiffness of four fixed-guided supporting beams of the actuator shaft is:

$$K_S = 4\frac{Ehw_{s1}^3}{L_{s1}^3} \quad (7)$$

where w_{s1} and L_{s1} are the width and length of the supporting beam. There are six fixed-guided supporting beams connected to the output side of the motion amplification mechanism; thus, the input stiffness of the mechanism, K_m, is determined by the compliance of the mechanism itself and the supporting beams [33]:

$$K_m = \left\{ -\frac{l_1}{l_2}K_{hinge}\left[\cos(\theta_1 + \theta_2) + \sin\theta_1\cos\theta_2\cot\theta_2\right] \right.$$
$$\left. -2K_{hinge} - \frac{Ew_a h^3}{12l_3} \right\} \frac{2\alpha}{l_0 l_1 \cos\theta_1} + 2Eh\left(\frac{w_{s2}^3}{L_{s2}^3} + 2\frac{w_{s3}^3}{L_{s3}^3}\right) \quad (8)$$

where w_a is the width of the flexible beam in the amplification mechanism, and K_{hinge} is the stiffness of the equivalent torsional spring in the amplification mechanism [33]. w_{s2}, w_{s3} and L_{s2}, L_{s3} are the widths and lengths of the supporting beams connected to the central stage ($\times 2$) and the central shaft on the other side of the central stage ($\times 4$). Substituting equations (6)–(8) into equation (2) and then combining equations (2), (3), and (5), the output displacement of the thermal actuator is thus obtained:

Table 1. Primary geometric parameters of the MEMS XY-stage.

l_0	75 μm	θ_2	170°
l_1	325 μm	L	500 μm
l_2	375 μm	l	25 μm
θ_1	20°	w	10 μm

$$U = \frac{2\gamma f_{23}LV^2}{\kappa\rho\left\{(f_{11}f_{23} - f_{12}f_{13})\frac{f_{33} - (f_{22}f_{33} - f_{32}f_{23})K}{f_{12}f_{33} - f_{13}f_{23}} + [(f_{12}f_{23} - f_{22}f_{13})K + f_{13}]\right\}} \quad (9)$$

The motion amplification mechanism has been demonstrated to be highly linear for displacement reduction [33], and the displacement of the center stage can thus be calculated by simply multiplying the output displacement of the thermal actuator U with the displacement minification ratio α. Omitting a detailed design process, the primary geometric parameters of the fabricated MEMS stage are summarized in table 1.

The Z-beam actuator is mechanically connected by the UV-curable glue filled in the electrical-insulation gaps. It is noted that the stiffness of the glue is generally smaller than that of silicon, and the deformation of the glue connection during actuation may therefore cause a variation in the displacement transmitted from the Z-beam actuator to the motion amplification mechanism or the capacitive displacement sensor. Denote the size of the insulation gap by w_g, the cross-sectional area of the input shaft by A_{sh}, and the Young's modulus of the cured glue by E_g, and assume that the insulation gap is completely filled by the glue and the temperature increase of the actuator shaft does not significantly affect the stiffness of the glue (confirmed in section 2.3). The relative error of the transmitted displacement by the glue-filled gap, defined as the ratio of the glue deformation (along the actuation axis) and the output displacement of the Z-beam actuator, can be derived as

$$\delta = \frac{Kw_g}{E_g A_{sh}}. \quad (10)$$

From equation (10), it can be noted that, with the selected geometric parameters of the stage (thus the selected K), the relative error δ is dependent on the Young's modulus of the glue (E_g) and the geometric parameters of the insulation gap (w_g and A_{sh}). Figure 3 shows the calculated relative error δ as a function of the gap size and the glue Young's modulus, using the K value determined by the geometric parameters in table 1. One can see that, in order to decrease the relative error δ, a high-stiffness glue and a small gap size should be adopted. In this design, we fabricated the gap to be 5 μm and chose a UV-curable glue (Loctite® 3335) with the Young's modulus of 100 MPa. The corresponding relative error δ is calculated to be 0.13% (figure 3), which can be neglected in experiments.

2.3. Multiphysics finite element analysis

The theoretical analysis in section 2.2 is based on the assumption of uniform temperature increase across the Z-shaped

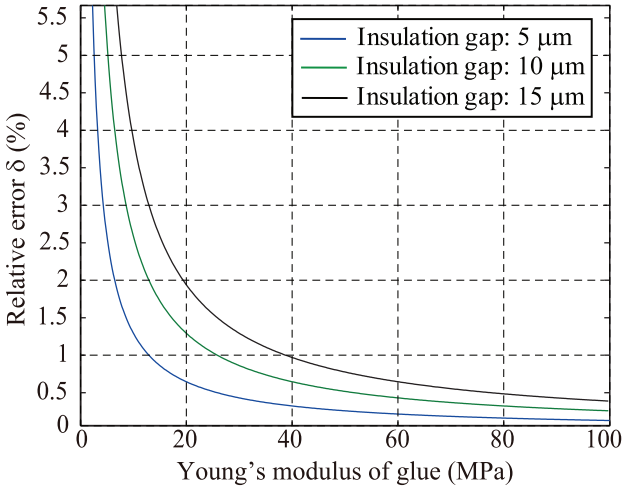

Figure 3. Relative error of the transmitted displacement by a glue-filled gap.

Table 2. Mechanical and thermal properties of single crystalline silicon.

Young's modulus, E	160 GPa	[37]
Silicon density	2300 kg m^{-3}	
Poisson's ratio	0.28	[37]
Thermal expansion coefficient	$\{3.725 * [1 - e^{-5.88\times10^{-3}(T-124)}] + 5.548 \times 10^{-4}T\} \times 10^{-6}$ °C^{-1}	[38]
Thermal conductivity	146 W m.K^{-1}	[39]
Electrical resistivity	1.8×10^{-4} Ω.m	Measured

beam as the input of the analytical model. However, due to thermal conduction, the actual temperature distribution on the Z-shaped beam always follows a certain gradient. Multiphysics finite element analysis (FEA) allows for the direct correlation of the actuation voltage and the output displacement of the Z-beam actuator, and is also able to provide the temperature and stress distributions on the device structures at different actuation voltages. We performed multiphysics FEA on single axis of the stage using ANSYS 15.0. A three-dimensional element SOLID 226 was used to couple the electrical, thermal, and mechanical fields, and the geometric and material parameters of the stage used in the FEA are summarized in tables 1 and 2. Only the thermal conduction from the Z-beam actuator to its anchors was considered in the FEA.

Figure 4(a) illustrates the temperature distribution in one axis of the MEMS stage when an actuation voltage of 10 V was applied to the Z-shaped beams for actuation along $-X$. It can be observed that the highest temperature occurred at the portion of Z-shaped beams near the central shaft of the actuator. The temperature of the central shaft was lower than the highest temperature due to the thermal conduction along the shaft. It was determined that, based on the FEA results, the temperature at the electrical-insulation gaps reaches to

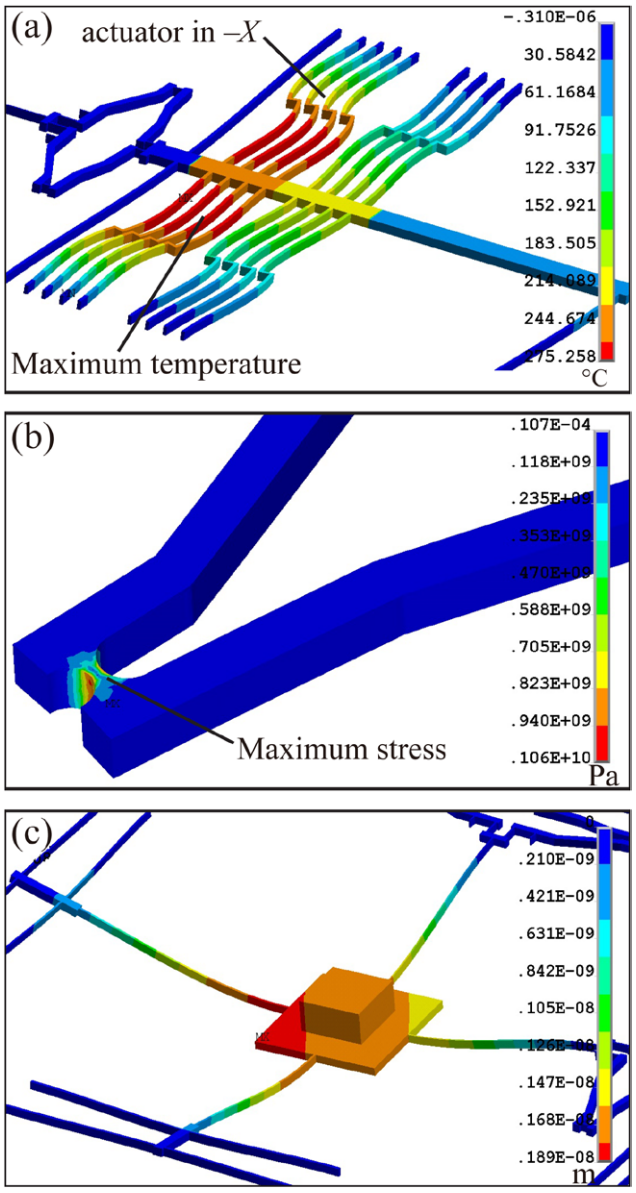

Figure 4. Finite element simulation results of the *XY*-stage. (a) Temperature distribution. (b) Stress distribution on the flexure hinge. (c) Deformation of the central stage carrying a silicon part of $200 \times 200 \times 100$ μm^3.

the limit of the operating temperature range of the glue at an actuation voltage 15 V. Thus, in order to avoid softening of the glue at higher temperatures, the *XY*-stage was only operated at the actuation voltage of 15 V. Within this limiting actuation voltage, the maximum stress of the stage structures was determined to be 1.06 GPa, which occurred at the hinges connecting the toggle and lever mechanisms (figure 4(b)). This maximum stress of 1.06 GPa is well below the yield strength of silicon (7 GPa) [40]. The load-carrying capacity of the stage was also studied in the simulation. When a silicon piece with sizes of $200 \times 200 \times 100$ μm^3 was loaded, the maximum deformation of the central stage is 1.89 nm (figure 4(c)). This level of out-of-plane deformation did not cause significant positioning errors in *X*- and *Y*-axes. Therefore the *XY*-stage is stiff enough for the manipulation of micro samples.

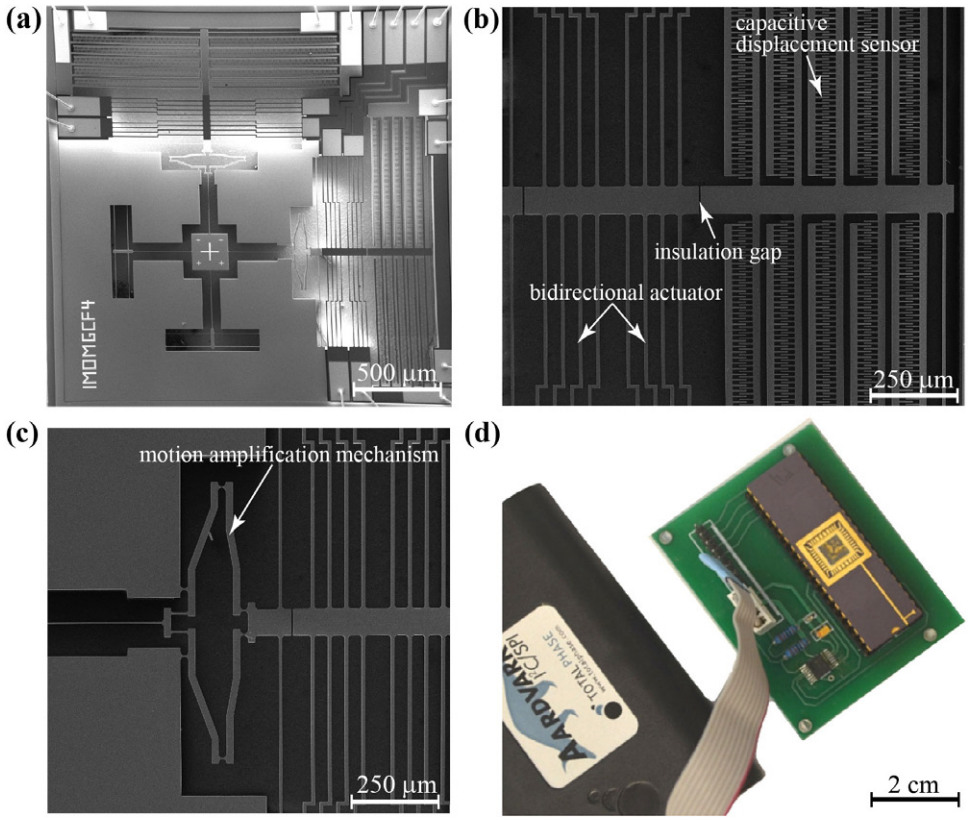

Figure 5. SEM photographs of (a) a released MEMS *XY*-stage and (b) and (c) zoomed-in views of the bidirectional electrothermal actuator, the motion amplification mechanism, and the capacitive displacement sensor. (d) Photograph of a *XY*-stage wire-bonded in a DIP40 package and its capacitive readout circuit.

3. Calibration results and discussion

Figure 5(a) shows a scanning electron microscopy (SEM) photograph of the MEMS *XY*-stage before adding the UV-curable glue to fill the electrical-insulation gaps. For device testing, the silicon chip was glued and wire bonded onto a ceramic DIP40 package, which was then inserted into a printed circuit board (PCB) with a dual-channel, capacitance-to-digital converter (AD7746, Analog Devices) for readout of capacitance values from the two displacement sensors. An inter-integrated circuit (I^2C) bus adaptor (Aardvark) was employed for data transmission from AD7746 to the host computer. The calibration experiments were performed on an anti-vibration table, at 21 °C and 50% relative humidity.

A DC power supply (Agilent, E3649A) was used to apply actuation voltages to the Z-beam actuators, and an upright microscope (BX-53, Olympus) with a 20 × objective and a digital camera (image size: 1623 × 1232 pixels) were employed for measuring the input and output displacements of the motion amplification mechanism and the displacements of the central stage. The pixel size was calibrated to be 219 nm/pixel. We used a sub-pixel autocorrelation algorithm (resolution: 0.08 pixel) [41] for further improving the displacement measurement resolution to be 17.5 nm.

Figure 6 shows the testing results of the Z-beam actuators along *X*- and *Y*-axes (the negative voltage values indicate they were applied to the Z-shaped beams actuating along $-X$ and $-Y$) directions. At 15 V, the Z-beam actuators produce displacements of 8.53 μm, 7 μm, 9.84 μm, and 8.31 μm along $+X$, $-X$, $+Y$, and $-Y$ directions, respectively. The actuator displacements calculated from the derived analytical model (equation (9)) agrees well with the experimental results with prediction errors of $\leqslant$25%. These prediction errors of the analytical model can be attributed to three possible reasons. (i) The analytical model assumes uniform temperature increases across the Z-shaped expansion beams when actuation voltages are applied; however, in the real case, there is always temperature distributions (figure 4) on the Z-shaped beams because of the heat transfer from the beams to the actuator anchors. (ii) The mechanical and electrical parameters (i.e. E, κ, and ρ) of silicon employed in calculation of the analytical model were obtained from the literature, and could have small deviations with the real parameter values of the device. (iii) There are also small dimensional differences of the device from the ideal design because of the imperfection of device microfabrication. In addition, we found that the measured forward and reverse displacements along both *X*- and *Y*-axes are not completely symmetric, which is probably due to small dimensional discrepancies of the Z-beams along the *X*- and *Y*-axes that cause slightly different buckling behaviors and electrical properties.

Figure 7 shows the linear relationship of the measured input and output displacements of the motion amplification mechanism, with a linearity of 11.3% and a reduction ratio of −0.1057. At 15 V, the maximum output displacements of the *XY*-stage were determined to be 901.6 nm in $+X$, 739.9 nm

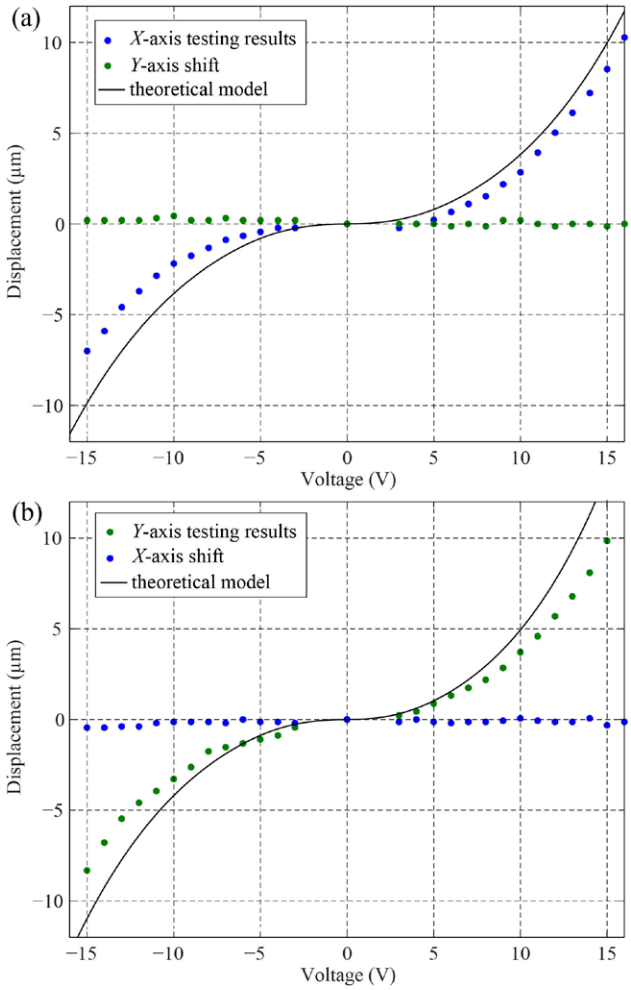

Figure 6. Calibration results of the Z-beam electrothermal actuators along (a) *X*- and (b) *Y*-axes.

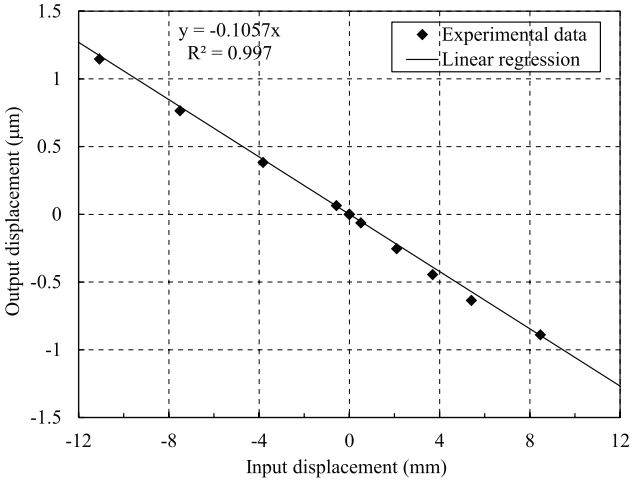

Figure 7. Experimental data of the input and output displacements of the motion amplification mechanism.

in $-X$, 1.04 μm in $+Y$, and 878.4 nm in $-Y$. Figure 8 shows the calibration results of the capacitive displacement sensor. One can see that the sensor has a linear capacitance output response along the forward direction ($+X$ or $+Y$), while its output along the reverse direction ($-X$ or $-Y$) is linear in a small displacement range (0–6.1 μm) but nonlinear in the whole displacement range of 0–10 μm. This observation can be explained by the fact that the parasitic capacitance of the interdigitated comb fingers become more significant when the movable fingers move along the reverse direction ($-X$ or $-Y$), thus causing a nonlinear behavior when the movable and stationary fingers are close (reverse displacement is large).

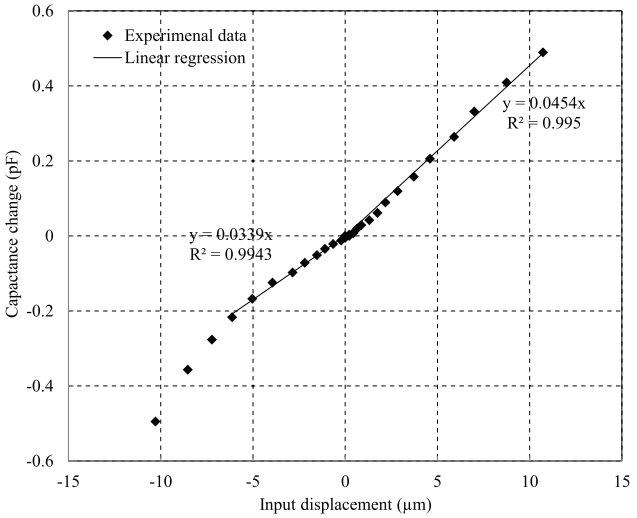

Figure 8. Calibration results of the capacitive displacement sensor. Displacement data in a small range of 0–6.1 μm was used for linear regression along the reverse direction.

The resolution of the capacitance readout circuit was determined to be 30 aF $\sqrt{\text{Hz}}^{-1}$ that corresponds to input displacement resolutions of 2.09 nm $\sqrt{\text{Hz}}^{-1}$ along the forward direction and 2.80 nm $\sqrt{\text{Hz}}^{-1}$ along the reverse direction. Because of the good input-output linearity of the motion amplification mechanism, its output displacement (at the central stage) can be accurately predicted from its input displacement (measured through the capacitive displacement sensor). Considering input displacement resolutions (2.09 nm $\sqrt{\text{Hz}}^{-1}$ along $+X$ and $+Y$, and 2.80 nm $\sqrt{\text{Hz}}^{-1}$ along $-X$ and $-Y$) and the motion reduction ratio (-0.1057; linearity: 11.3%), the output displacement resolutions of the *XY*-stage were determined to be 0.22 ± 0.0025 nm $\sqrt{\text{Hz}}^{-1}$ along and $+X$ and $+Y$ and 0.30 ± 0.0033 nm $\sqrt{\text{Hz}}^{-1}$ along $-X$ and $-Y$.

Using the capacitive displacement feedback, we demonstrated closed-loop control of the output displacements of the *XY*-stage based on the proportional-integral-derivative (PID) control law. The sampling frequency of the position feedback was 20 Hz (limited by the capacitance readout chip—AD7746), and the PID controller parameters were optimized through trial-and-error experiments. Figure 9 shows the tracking result of the *XY*-stage following a circular path with a diameter of 200 nm. The tracking path of the *XY*-stage shows small deviations at the zero points of *X*- and *Y*-axes, which arose from the structural buckling instability of the Z-shaped beams (that is, the two long sub-beams of the Z-beam need to be first buckled, at zero displacement output, to bend the Z-beam). Implementing a model-based controller [25] and introducing control strategies for vibration suppression [42] could effectively reduce these beam-buckling-induced tracking errors.

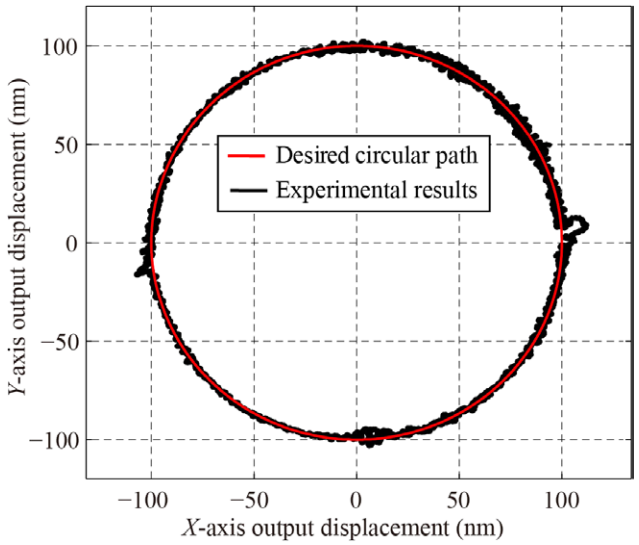

Figure 9. Experimental results of closed-loop circular tracking.

Choosing a capacitance readout chip with a higher sampling frequency (e.g. MS3110, MicroSensors) will also improve the system's dynamic response and thus further reduce the tracking errors.

4. Conclusion

This paper presented a MEMS nanopositioning *XY*-stage utilizing compliant motion amplification mechanism for improving the stage's positioning resolution to the sub-nanometer level. Z-beam electrothermal actuators were used to produce micrometer displacements which were further reduced by the motion reduction mechanism by a constant factor. A capacitive displacement sensor was used to measure the input displacement of the motion amplification mechanism with nanometer measurement resolution. An analytical mechanics model was developed to predict the output displacement of the *XY*-stage as a function of the input voltage, providing useful device design guidelines. The motion amplification mechanism was experimentally proved to have a linear input-output relationship (linearity: $\leqslant$11.3%), and the resolution of the stage's output displacement were determined to be 0.22 ± 0.0025 nm $\sqrt{\text{Hz}}^{-1}$ along and $+X$ and $+Y$ and 0.30 ± 0.0033 nm $\sqrt{\text{Hz}}^{-1}$ along $-X$ and $-Y$. Closed-loop PID control of the *XY*-stage was also demonstrated. With the enhanced sub-nanometer positioning resolution, the developed *XY*-stage could be used for fine positioning on top of a regular piezoelectric stage for high-resolution sample positioning under SPMs or SEMs.

Acknowledgments

This work was supported by Natural Sciences and Engineering Research Council of Canada (NSERC; grant no. RGPIN 418553-12), Canada Foundation for Innovation (CFI; grant no. CFI-LOF 30316), and McGill University (grant no. 234304). The authors also acknowledge supports from the Canada Research Chairs Program (to X Liu; grant no. 237293) and the China Scholarship Council (to X Xi).

References

[1] Yong Y, Moheimani S, Kenton B J and Leang K 2012 *Rev. Sci. Instrum.* **83** 121101
[2] Yong Y K, Bhikkaji B and Moheimani S R R 2013 *IEEE/ASME Trans. Mechatronics* **18** 1060–71
[3] Ra H, Piyawattanametha W, Taguchi Y, Lee S, Mandella M J and Solgaard O 2007 *J. Microelectromech. Sys.* **16** 969–76
[4] Takahashi K, Mita M, Fujita H and Toshiyoshi H 2006 *IEICE Electron. Express* **3** 197–202
[5] Langfelder G, Caspani A and Tocchio A 2014 *IEEE Trans. Ind. Electron.* **61** 567–74
[6] Kwon H N, Lee J H, Takahashi K and Toshiyoshi H 2006 *Sensors Actuators* A **130** 468–77
[7] Fan L, Wu M, Choquette K D and Crawford M H 1997 Self-assembled microactuated xyz stages for optical scanning and alignment *Proc. Int. Conf. Solid State Sensors and Actuators* vol **1** pp 319–22
[8] Xu Y, MacDonald N and Miller S 1995 *Appl. Phys. Lett.* **67** 2305–7
[9] Ando Y 2004 *Sensors Actuators* A **114** 285–91
[10] Mohammadi A, Fowler A G, Yong Y K and Moheimani S R 2014 *J. Electromech. Syst.* **23** 610–9
[11] Dong J and Ferreira P M 2009 *J. Microelectromech. Syst.* **18** 641–51
[12] Sun L, Wang J, Rong W, Li X and Bao H 2008 *J. Micromech. Microeng.* **18** 125004
[13] Liu X, Kim K and Sun Y 2007 *J. Micromech. Microeng.* **17** 1796
[14] Kim Y S, Dagalakis N G and Gupta S K 2013 *J. Micromech. Microeng.* **23** 055008
[15] Kim C H, Jeong H M, Jeon J U and Kim Y K 2003 *J. Microelectromech. Syst.* **12** 470–8
[16] Eleftheriou E *et al* 2003 *IEEE Trans. Magn.* **39** 938–45
[17] Choi J J, Park H, Kim K Y and Jeon J U 2001 *Proc. SPIE* **4334** 363–71
[18] Pandey A, Pratap R and Chau F 2008 *Exp. Mech.* **48** 91–106
[19] Chen S C and Culpepper M L 2006 *Precis. Eng.* **30** 314–24
[20] Mukhopadhyay D, Dong J, Pengwang E and Ferreira P 2008 *Sensors Actuators* A **147** 340–51
[21] Kim Y S, Yoo J M, Yang S H, Choi Y M, Dagalakis N G and Gupta S K 2012 *J. Micromech. Microeng.* **22** 085029
[22] Lin C Y, Tsai T Y and Chiou J C 2011 *IEEE 4th Int. Nanoelectronics Conf.* (Piscataway, NJ: IEEE) pp 1–2
[23] Hubbard N B and Howell L L 2005 *J. Micromech. Microeng.* **15** 1482
[24] Ji L, Zhu Y, Moheimani S R and Yuce M R 2010 A micromachined 2DOF nanopositioner with integrated capacitive displacement *IEEE Int. Conf. Sensors* (Piscataway, NJ: IEEE) pp 1464–7
[25] Rakotondrabe M, Fowler A G and Moheimani S R 2014 *IEEE Trans. Control Syst. Technol.* **22** 1486–97
[26] Guan C and Zhu Y 2010 *J. Micromech. Microeng.* **20** 085014
[27] Ouyang J and Zhu Y 2012 *J. Microelectromech. Syst.* **21** 596–604
[28] Zhu Y, Moheimani S R and Yuce M R 2012 *IEEE Sensors J.* **12** 2508–9
[29] Moore S and Moheimani S 2014 *J. Microelectromech. Syst.* **23** 511–3
[30] Millet O, Bernardoni P, Régnier S, Bidaud P, Tsitsiris E, Collard D and Buchaillot L 2004 *Sensors Actuators* A **114** 371–8
[31] Lin L, Pisano A P and Howe R T 1997 *J. Microelectromech. Syst.* **6** 313–21

[32] Chu L L and Gianchandani Y B 2003 *J. Micromech. Microeng.* **13** 279
[33] Liu X, Tong J and Sun Y 2007 *Smart Mater. Struct.* **16** 1742
[34] Chu C L and Fan S H 2006 *Precis. Eng.* **30** 85–95
[35] Kim K, Liu X, Zhang Y, Cheng J, Wu X Y and Sun Y 2009 *Biomed. Microdev.* **11** 421–7
[36] Hickey R, Kujath M and Hubbard T 2002 *J. Vac. Sci. Technol.* A **20** 971–4
[37] Zhu Y, Moldovan N and Espinosa H D 2005 *Appl. Phys. Lett.* **86** 013506
[38] Okada Y and Tokumaru Y 1984 *J. Appl. Phys.* **56** 314–20
[39] Geisberger A A, Sarkar N, Ellis M and Skidmore G D 2003 *J. Microelectromech. Syst.* **12** 513–23
[40] Peterson K E 1982 *Proc. IEEE* **70** 420–57
[41] Bing P, Hui-Min X, Bo-Qin X and Fu-Long D 2006 *Meas. Sci. Technol.* **17** 1615
[42] Boscariol P and Zanotto V 2012 *Robotica* **30** 15–29